Fire Safety Journal 91 (2017) 91–102

Contents lists available at ScienceDirect

Fire Safety Journal

journal homepage: www.elsevier.com/locate/firesaf

IAFSS 12th Symposium 2017

Stochastic modeling of firebrand shower scenarios

Ali Tohidi[a,*], Nigel B. Kaye[b]

[a] Department of Fire Protection Engineering, University of Maryland at College Park, J.M. Patterson Building, College Park, MD 20740, USA
[b] Department of Civil Engineering, Clemson University, Glenn Department of Civil Eng. South Palmetto Blvd, Clemson, SC 29634, USA

ARTICLE INFO

Keywords:
Firebrand
Wildfire
Stochastic modeling
OpenFOAM
LES
Wind tunnel

ABSTRACT

Firebrand shower and its subsequent spot fires are responsible for more than half of the ignitions reported during wildfires, in particular at wildland urban interface (WUI) areas. The firebrand transport is a highly stochastic and nonlinear problem which directly influences the spotting distribution. Hence, a coupled stochastic model of firebrand showers, that is thoroughly and systematically validated against large scale wind tunnel experiments of lofting and downwind transport of model firebrands, is presented. It is shown that the developed model predicts the first and second order statistics of the flight accurately in relation to the experimental data. The sensitivity of the model to the initial conditions of the flight as well as the velocity field characteristics are examined.

1. Introduction

Detrimental consequences of Climate Change such as rise in temperature, more severe and frequent droughts, and changes in precipitation patterns, as well as soil moisture index, have made wildfires a more extreme and ubiquitous phenomenon throughout the globe [1]. Each year, on average, wildfires burn millions of acres of land not only in the United States [2] but also in other parts of the world such as Iran where, more than 6% of the forests are being destroyed by them [3]. Regardless of the ecological and social impacts of wildfires, they expose people, properties, and infrastructure to a great threat. Unfortunately, recent land development trends at the wild-land urban interface (WUI) have drastically increased these risks and their associated costs [1,2,4]. Apart from the economic burden, once a wildfire happens the main responsibility is to contain and protect people, property, and mitigate the effects. To this end, understanding wildfire spread mechanisms is of paramount importance. The three pathways by which wildfires propagate are convective heat transfer (direct flame impingement on the fuel sources), radiant exposure (ignition of fuels/vegetation adjacent to large flames), and firebrand shower [2]. While convective and radiant heat transfer may propagate fire through forests, recent studies suggest that exposure to firebrand showers, particularly in WUI communities, is the main cause of fire spread [1,2,5].

Firebrand shower also known as fire spotting is a convoluted multi-physics phenomenon that consists of three stages; first, firebrand formation and breakage from burning vegetation or wooden elements, second, lofting and downwind transport of these firebrands through the wildfire plume envelope and atmospheric boundary layer, and finally, ignition of spot fires upon landing on fuels [6]. Fig. 1, illustrates a schematic of the firebrand shower phenomenon. A variety of parameters such as the size, shape, number, and mass (flux) of firebrands, as well as the moisture content of the fuel bed, terrain characteristics, meteorology, and exposure time to radiant and convective heat fluxes from firebrands [7] are involved in estimating the susceptibility of a region to spot fires. Among various stages and agents that affect fire spotting, firebrand flight is a highly complex stochastic process that strongly influences the maximum downwind transport of firebrands. Hence, the lofting and downwind transport has been extensively studied compared to other stages, namely firebrand generation and spot fire ignition.

To date, most transport models are extensions of the work of Tachikawa [8,9] on debris flight models, which characterizes the transport based on the mass and shape of particles with a set of nonlinear momentum equations. Due to aerodynamic complexities, transport models, specifically, for compact (spherical) [10,11], plate-like, and rod-like [12,13] particles have been developed. However, application of these models to the firebrand shower problem has not been promising as many simplified assumptions were involved in the model development procedure. For instance, customarily in previous studies [14–17], it is assumed that the relative velocity vector is either always normal to the largest area of firebrands, in order to estimate the maximum flight distance, or is aligned with their principal axis. Consequently, this automatically eliminates/reduces the side lift force, and converts the three-dimensional (3D) trajectory of firebrands to two-dimensional (2D), despite 3D motion being an observed flight

* Corresponding author.

http://dx.doi.org/10.1016/j.firesaf.2017.04.039
Received 14 March 2017; Received in revised form 20 April 2017; Accepted 21 April 2017
Available online 04 May 2017
0379-7112/ © 2017 Elsevier Ltd. All rights reserved.

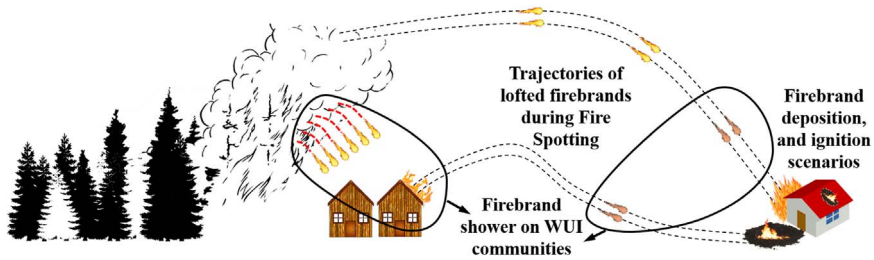

Fig. 1. Schematic of the firebrands shower exposure and its role in wildfire spread within WUI communities.

characteristic of these objects [18]. Others [19–21] reduce the order of aerodynamic complexity by assuming compact form for firebrands/debris in their particle transport models, although there is a growing body of experimental and field observations that thin disks and rod-like (cylindrical) forms are the most common shapes of firebrands generated from WUI fires [6,4]. Also, Koo et al. [22] argues that the compact model is the most difficult shape of a given mass to get lofted through the fire plume. Collectively, there has been limited work done on firebrands with non-compact forms [1,23].

On this matter, there exist some studies [6,15,16,24] where either the time-averaged velocity field of a fire plume through the boundary layer cross-flow was used or firebrands (mostly disk-shape) were released from a certain height through a uniform time-averaged boundary layer, i.e. lofting and downwind transport were decoupled. With regard to cylindrical-shape firebrands, the aerodynamic force coefficients were measured by Marte et al. [25], over a limited range of parameter space, and adopted in a six-degree-of-freedom (6-D.O.F.) transport model by Radbill and Redman [26]. For rod-like debris, there is very limited literature [27–29] available which in almost all of them the flight characteristics are measured or modeled solely based on the angle of attack, that is the tilt angle has been ignored. Nonetheless, in a series of influential wind tunnel experiments Richards et al. [13], Richards [30] measured the steady aerodynamic force and moment coefficients of plate-like and rod-like objects in terms of variations in both the angle of attack and the tilt angel. These results were, then, incorporated to a deterministic three-dimensional 6-D.O.F. numerical transport model and, qualitative comparisons between the simulated trajectories and wind tunnel experiments were presented. Later, Richards [31] showed that although the aerodynamic force and moment coefficients might change by either rotation of the projectiles or turbulent characteristics of the velocity field, unsteady force and moment coefficients are only important for early stages of the flight where the accelerations are high. Therefore, plate and rod-like firebrand (debris) transport models that are developed using steady aerodynamic force and moment coefficients [30,32] are likely to account for the complete flight behavior and may deliver accurate results with high confidence levels, namely proper estimation of the first and second order statistics of the trajectories. Indeed, this is crucial as the downwind travel distance, i.e. ground distribution of firebrands or potential spotting distribution [33], is a very important measure in assessing the likelihood of spot fire occurrence in a fire prone area. Hence, given that the firebrand transport is naturally a highly stochastic and nonlinear phenomenon and reliability of the estimated risks as well as the decision making costs associated with firebrand showers are dependent on properties of the spotting distribution [1,33], adopting a probabilistic approach is necessary. This is achieved, here, by adopting the deterministic transport model of Richards [30] and implementing it to a stochastic modeling approach. In fact, prior to this process, the transport model has been experimentally validated through Metropolis Monte-Carlo simulations of the free-fall experiments conducted; see Tohidi [23]. Details of the free-fall experiments as well as the validation process, where it is shown that the transport model is capable of predicting the first and second order statistics of the firebrands' (debris) flight such that the simulation results are not statistically significantly different from the free-fall experiments [23], are not within the scope of this study.

Regarding stochastic modeling, although physics-based probabilistic models [33–35] are available, similar to almost all of the previous works on fire spotting, they suffer from either decoupling lofting from downwind transport or lack of thorough experimental validation. In fact, except very few studies [17] with limited parameter space, there was no experimental data set for evaluating the performance of existing firebrand (debris) transport models through firebrand shower scenarios, even for Richards [30] model. However, the lack of experimental data gap is covered by conducting the most comprehensive set of lofting and downwind transport of non-combusting rod-like model firebrands, with different aspect ratios, through large scale wind tunnel experiments; see [1, chapter 5]. Given the availability of experimental data and a deterministic transport model, which is capable of modeling flight characteristics provided that a sufficient subset of the ensemble of transport is simulated, the main objective of the present study is to develop a coupled stochastic parametric model for firebrand transport and, systematically evaluate its performance using wind tunnel data of Tohidi and Kaye [1]. In this regard, the Monte-Carlo type simulation results of this model, which couples the Large Eddy Simulation (LES) resolved velocity field induced by the interaction of the fire plume and atmospheric boundary layer with a 3D deterministic 6-D.O.F. firebrand flight model [30], are presented. The experimentally validated stochastic model not only provides better understanding of the firebrand flight but also paves the way towards development of advanced classifiers which eventually lead to a more reliable fire spotting risk estimation. Moreover, the discussed methodology and findings here, as well as the experimental data on model firebrands' flight by Tohidi and Kaye [1], may be invaluable for modeling debris/particle transport within other extreme events such as hurricanes, storms, and tornadoes. The remaining parts of this study are organized in the following way. In the next Section 2 the model development and methodology as well as the wind tunnel experiments of Tohidi and Kaye [1] are described. The results and discussions are then presented followed by concluding remarks.

2. Model development

This section describes the development procedure of a coupled stochastic parametric model of firebrand transport. However, it is necessary to present a brief overview of the large scale wind tunnel experiments of the firebrand shower scenarios, as their data is employed to validate the model.

2.1. Wind tunnel experiments

Boundary layer wind tunnel experiments of fire spotting were run using non-combusting polyurethane model firebrands with density $\varrho = 30\ \mathrm{kg/m^3}$, side aspect ratio $\eta_s = L_x/L_y = 1$, and different longitudinal aspect ratios of, i.e. $\eta = L_z/L_{x,y} = 1$, 4 and 6, as shown in Fig. 2-(a). The dimension of all sides in the $\eta = 1$ model firebrands were $L_x = L_y = L_z = 1$ cm and for other aspect ratios $L_x = L_y = 0.5$ cm. The tests were conducted in Clemson University's wind tunnel testing

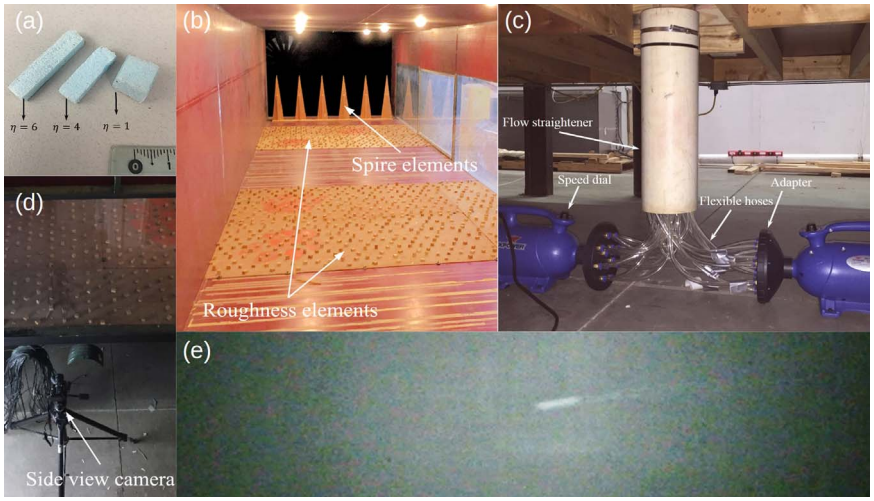

Fig. 2. Shown is the wind tunnel experiments setup including (a) polyurethane-made firebrand models and the 1 cm length scale, (b) inside the wind tunnel chamber where the surface roughness and spire elements are installed, (c) details of the mounted air jet underneath of the wind tunnel test section along with blowers, and the flow straightener, (d) the camera and filming position at the side view of the release point, and (e) a side view from a rod-like firebrand model during flight from left to right.

facility, see Fig. 2-(b,c), which its test section is comprised of a 3.00 m wide by 2.03 m high open boundary layer with 20 m of fetch. In order for the boundary layer to be turbulent, a combination of spire boards and surface roughness elements were used as shown on Fig. 2-(b). The velocity field of the fire plume was modeled using an air jet installed underneath of the wind tunnel floor; see Fig. 2-(c). The 15.2 cm diameter jet was created using two 4 hp blowers that were fed into a 58.8 cm flow straightener. The jet centerline exit velocity could be adjusted between $0 - 12$ m/s.

In order to model the velocity field induced by the interaction of the fire plume and the boundary layer, experiments were run for combinations of three boundary layer reference velocities, i.e. $U_0 = 1.79$, 2.23 and 2.85 m/s, and three jet centerline velocities, namely $U_{j|r=0} = 8.05$, 9.0, and 12 m/s. Given that the maximum centerline velocity of the jet, is relatively low in relation to the velocity field of a typical wildfire, the choice of a low density material for the model firebrands assures them getting lofted and, provides a better approximation in terms of scaling the phenomenon in wind tunnel experiments. The use of a different density material in debris flight modeling is common with the Tachikawa number [36] being used to re-scale the results to different density debris. The sixty second time-averaged velocity profiles of the boundary layer at centerline of the wind tunnel's test section, as well as the cross-sectional and vertical velocity profiles of the jet nozzle exit are shown in Fig. 3. The associated uncertainties with velocity measurements shown in Fig. 3 are not presented, as they are, at most, less than 3.33% and 1.25% for the boundary layer and jet, respectively.

It should be noted that complete scale similarity, that is geometric, kinematic, and dynamic similarity, between the experiments and wildfires cannot be achieved. Very little is known about the size and shape of the generated firebrands through real wildfires and laboratory studies exhibit a broad range of sizes and shapes [1,4,37–39]. Therefore, complete geometric similarity would require an unfeasible number of experiments. Also, the dynamic similarity would not be possible as it requires pool fires to be made in wind tunnels (not possible in wooden wind tunnel of Tohidi and Kaye [1]) and then the wind speed should be scaled to match both the Froude number and the plume to wind velocity ratio; see Tohidi and Kaye [40]. For small laboratory fires this requires a boundary layer with very low bulk reference velocity that is not in the fully rough turbulent regime. Thus, geometric and dynamic similarity cannot be satisfied even if the largest available wind tunnels were being employed. Rather than simulating a buoyant fire plume we use an analogous antisymmetric turbulent shear flow, the round turbulent jet. This approach provides a valid alternative for model validation as the structure of the flows is qualitatively similar and the buoyancy force acting on the model firebrands is negligible compared to their weight such that temperature difference will have little effect on the flight. Further, the goal of this paper is to present a method for modeling the lofting and transport of model firebrands that is validated by laboratory scale experiments. This will allow future research to extend this modeling approach to include buoyancy effects with confidence in the validity of the underlying approach.

Given the scaling difficulties, different combinations of the wind tunnel boundary layer velocity with the vertical turbulent jet velocity were tested and modeled that were equivalent to the flow interaction of fire in the atmospheric boundary layer. Through the generated velocity fields different aspect ratios of the rod-like polyurethane model firebrands were released within roughly the centerline of the jet exit while their initial release (Tait-Bryan) angles changed randomly. In order to provide sufficient samples (degrees of freedom) of the lofting and downwind transport phenomenon, each aspect ratio was released approximately 200 times through the given velocity field. The entire trajectory of model firebrands was filmed at 60 frames per second from the side view, using a *GC-PX 100, JVC* camera. A particle tracking image processing algorithm was, then, developed in order to capture the full trajectory of model firebrands as shown below in Fig. 4-(left). The most striking result of the wind tunnel experiments, as shown on Fig. 4-(right), is that PDFs of the normalized downwind distance (x_l) with the maximum lofted height (z_{max}) are similar through each combination of the velocity field, regardless of the aspect ratio of the released firebrands. This signifies a very important fact that the landing location of firebrands through the boundary layer (maximum downwind distance) is positively correlated with the maximum rise height during the lofting phase in the fire plume envelope. Although the mean value of x_l/z_{max} is almost the same for all aspect ratios, the standard deviation of the normalized maximum downwind distance is to some extend dependent on the aspect ratio. In fact, larger aspect ratio firebrands are not only prone to more aerodynamic instability, due to rotational effects and subsequently variations in the center of pressure, but also they have larger projected surface area against the flow field which increases the magnitude of aerodynamic force relative to the gravity force, i.e. increase in the Tachikawa number [36], and leads to more variations in the spotting distribution as shown in Fig. 4-(right). Nonetheless, similarity of x_l/z_{max} PDFs indicates that the lofting and downwind transport cannot be decoupled. Also, the necessity of coupling the plume with the atmospheric boundary layer in modeling wildfire velocity field is shown by Tohidi and Kaye [40], as it directly affects the bent-over plume rise height and subsequently the travel

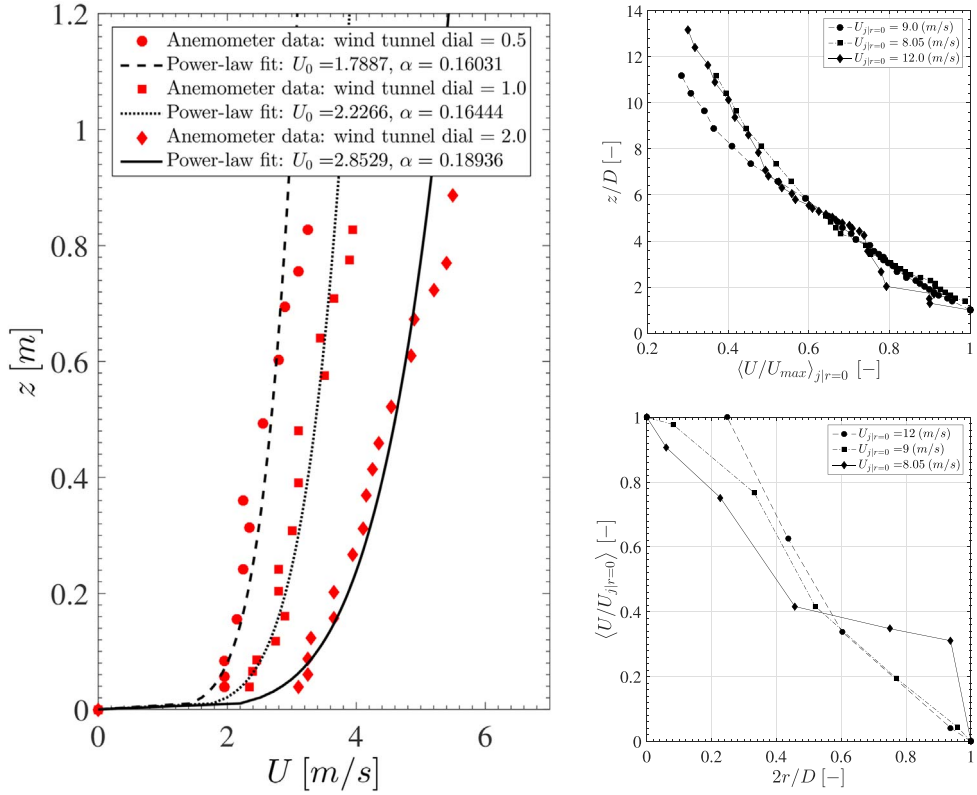

Fig. 3. (Left) Measured boundary layer velocity profiles at 0.25 m upstream of the jet entrance to the test section; also, shown are the corresponding power-law fits with U_0 as the horizontal velocity at the reference height z_0 = 0.04 m, and α the power-law fit exponent. (Right) Sixty second time-averaged normalized velocity profiles of the jet ($<U/U_{max}>_{j|r=0}$) along the z-direction, normalized with the jet diameter D, at the centerline (top); and the normalized radial direction of the jet cross section ($2r/D$) (bottom). Jet velocity measurements were carried out at z = 0.138 m from the nozzle exit, where the flow enters the test section.

distance of firebrands.

These findings suggest that in previous studies [17,19,21,24,41], which effectively only account for either lofting or downwind propagation and release of firebrands from an arbitrary height through the velocity field, there should be reasonable justifications for the adopted release heights, as it will have significant influence on the spotting distribution. Hence, a reasonable solution to these issues may be accomplished by coupling a firebrand transport model with an atmospheric dynamic model, which accounts for the detailed spatial and temporal scales of the velocity field induced by the interaction of the fire plume and the boundary layer. The obtained velocity fields can be utilized in stochastic modeling of firebrand shower phenomenon. While the modeling procedure is explained in the next section, for thorough details of the wind tunnel experiments and results, in particular, the data acquisition method and the particle tracking package refer to Tohidi and Kaye [1], Tohidi [23].

2.2. Transport model

In transport of non-compact particles, rotational effects are very important, in that they may lead to highly convoluted 3D trajectories. Therefore, in modeling firebrand showers, it is crucial to use a transport model which does account for these effects as most of the firebrands generated from burning vegetation are observed to be in rod-like and cylindrical forms [6]. As discussed, the Richards [30]'s model is adopted in that it is a fully deterministic 3D 6-D.O.F. model

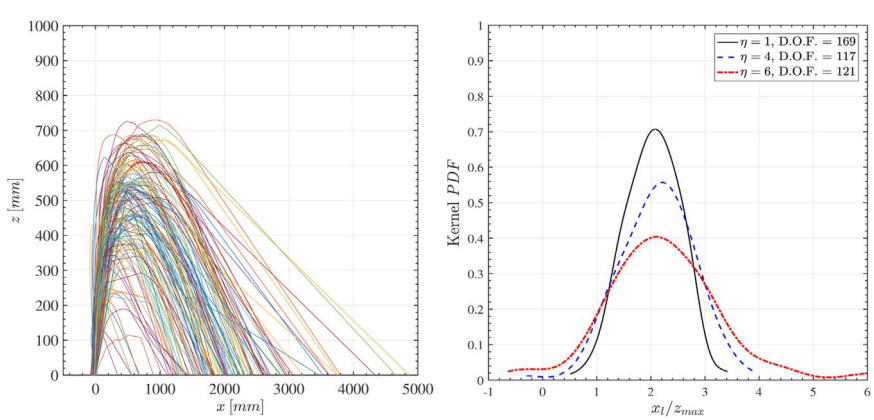

Fig. 4. Shown are sample results of the wind tunnel experiments. (Left) trajectories of the model firebrands with aspect ratio η = 6 released through the jet, with 12 m/s centerline velocity ($U_{j|r=0}$), entering the boundary layer cross-flow with 2.85 (m/s) reference velocity (U_0); (right) the empirical (kernel) probability density functions (PDF) of the landing location of firebrands (x_l) normalized with the maximum lofted height (z_{max}), for different aspect ratios, through the velocity field generated by $U_{j|r=0}$ = 8.05 m/s, and U_0 = 1.79 m/s. Here, D.O.F. stands for the number of resolved trajectories by the image processing algorithm, which corresponds to the degrees of freedom in statistical analysis.

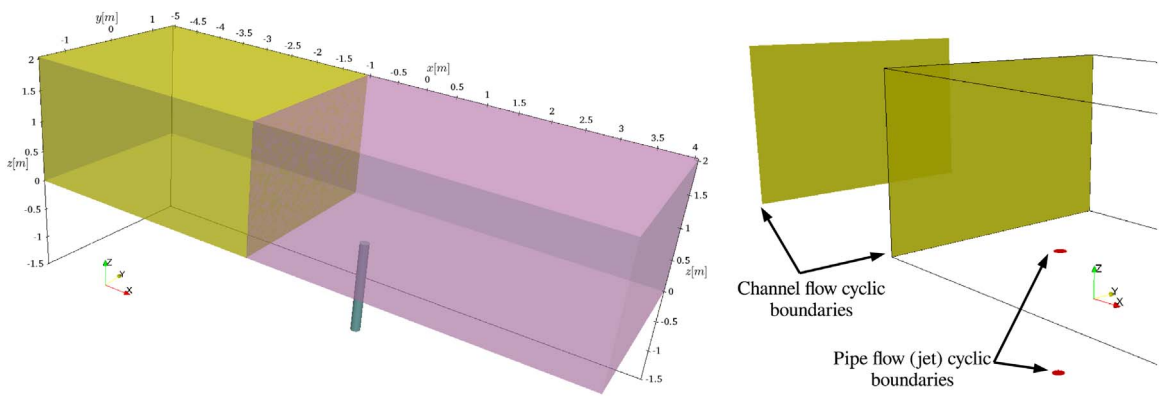

Fig. 5. Illustrated is the computational domain (left) and cyclic boundaries of the precursor domains (right). On the left, (Color version) the pink rectangular prism is the wind tunnel's test section where the model firebrands are released from the nozzle exit of the jet which its precursor pipe flow domain is shown by the blue cylinder, and the yellow (smaller) rectangular prism is the precursor channel flow domain. (For interpretation of the references to color in this figure legend, the reader is referred to the web version of this article.)

that accounts for the rotational effects of rod-like firebrands and, is experimentally shown that it can predict first and second order statistics of the flight provided that a subset of transport ensemble with sufficient number of samples is simulated, using Monte-Carlo type simulations.

Since the shape of firebrands does not change significantly after being charred [42], adding a reliable time-dependent combustion model, that accounts for the mass-loss, to the transport model is relatively straightforward. Also, as argued, most of the issues with modeling fire spotting are related to the aerodynamics of the flight rather than the combustion (mass-loss) effects which can be effectively addressed using proposed mass and shape distributions of firebrands by Tohidi et al. [4]. From these distributions, model firebrands with different mass and aspect ratios can be generated randomly and then released through the velocity field. Therefore, the transport model can account for the combustion effects such as mass-loss and different aspect ratios of firebrands as well. However, given the fact that the aforementioned wind tunnel experiments are being simulated, currently, the transport model is decoupled from the combustion effects as well as buoyant forces in the fire plume. This is consistent with the primary objective of this study. Hence, the governing equations of the firebrand flight, i.e. the linear and angular momentum equations, are respectively,

$$\ddot{\mathbf{x}} = \frac{1}{m}\mathbf{f} - g\mathbf{j} \tag{1}$$

and

$$\dot{\mathbf{L}}_\mathbf{p} = \mathbf{M}_\mathbf{p} - \boldsymbol{\omega} \times \mathbf{L}_\mathbf{p}. \tag{2}$$

In Eq. (1), $\ddot{\mathbf{x}}$ is the acceleration vector of the firebrands in a global translating but non-rotating coordinate system (see Grayson et al. [32]), $\mathbf{f}$ is the resultant force vector that is acting on the particle, m is the firebrand's mass, g is the gravity acceleration, and $\mathbf{j}$ denotes the unit vector along the vertical direction of the global coordinate system. Calculation of the resultant force vector ($\mathbf{f}$) is dependent on the orientation of firebrands with respect to the global coordinate system. Therefore, forces along principal components should be mapped to the global coordinate systems. This can be achieved using the transformation matrix $\mathbf{T}(\theta_x, \theta_y, \theta_z)$ where θ_x, θ_y and θ_z are "roll-yaw-pitch" angles in the Tait-Bryan convention [32], respectively. In addition, $\mathbf{f}$ is a function of relative velocity components along the principal axis of the firebrands and, the aerodynamic force coefficients which are themselves a function of the angle of attack, tilt angle, and geometric characteristics of the firebrands. In Eq. (2), $\mathbf{L}_\mathbf{p}$ denotes the angular momentum, $\mathbf{M}_\mathbf{p}$ is the vector of the applied moments about the object's principal axes, and $\boldsymbol{\omega}$ is the vector of angular velocity. It should be noted that for the angular momentum equation, rotational effects do not need to be transformed to the global coordinate system and can be directly calculated by utilizing Euler's rigid body dynamics equations [13,32]. The moment vector is, also, a function of firebrand velocity along the principal axes and the aerodynamic moment coefficients which are dependent on firebrand geometry, angle of attack and tilt angle; see [13]. More details on the transport model and integration methods through time can be found in either Richards et al. [13] or Grayson et al. [32].

The transport Eqs. (1) & (2) are nonlinear [13,32] which suggests that firebrands' flight may be highly sensitive to the initial conditions, namely break-off prior to the onset of lofting through the fire plume envelope. This implies that a little change in initial conditions may cause a significant difference in trajectory of the firebrands and subsequently the spotting distribution. In fact, nonlinearity of the equations is another reason, one must use a stochastic approach. This issue is addressed through a set of numerical experiments that correspond to the free-fall experiments mentioned before. It is found that the transport model [13] is highly sensitive to the initial release angles, i.e. Tait-Bryan angles, and after sufficient number of samples in the Monte-Carlo simulations the mean and standard deviation of the model converge to the corresponding free-fall experiments. The next section deals with details of replicating the velocity field of the wind tunnel experiments, where model firebrands travel through, with adequate temporal and spatial resolution.

2.3. Resolving velocity field

The flow field consists of two canonical wall-bounded flows. A fully developed channel flow that models the wind tunnel boundary layer and, a fully developed pipe flow which simulates the flow of the jet through the flow straightener. Interaction of these flows makes a jet in the boundary layer cross-flow which is qualitatively similar to the velocity field of a wildfire. The velocities in Cartesian coordinate system are (U, V, W) with fluctuations (u, v, w). The computational domain is shown in Fig. 5, where its streamwise length $l_x = 5$ m, spanwise length $l_y = 3$ m, height $h = 2.032$ m, and the initial kinematic viscosity of air is $\nu = 1.568 \times 10^{-5}$ m^2/s. Since wildfire plumes (velocity fields) are turbulent, the velocity fluctuations play an important role in the lofting capacity and subsequently spotting distribution of firebrands [21] and in general debris [43], as it is shown later in this study. This necessitates the proper spatial and temporal resolution of the velocity field. While the nature of the velocity fluctuations in a fire plume and air jet may differ, the goal of the model presented herein is to replicate the wind tunnel experiments described and, as such, the model simulation uses a constant density air jet. In order to capture the velocity fluctuations in the air jet the Large Eddy Simulation method [44], hereafter LES, is utilized for resolving the temporal and spatial scales of the flow. LES is adopted since it decomposes the flow scales into the large or grid-scale (GS) components and the small or sub-grid

scale (SGS) components, and makes using fairly coarse computational meshes possible as well as large time-steps [45]This has lower computational costs compared to Direct Numerical Simulation (DNS) methods while providing a significantly better spatial and temporal resolution relative to Reynolds-Averaged Navier-Stokes Simulations (RANS), i.e. time-averaged methods.

2.3.1. Governing equations & turbulence modeling

Since the problem is decoupled from any thermal effects, an incompressible isothermal viscous fluid model, which can be describe by the momentum and mass conservation equations, governs the flow. For more details on the flow's governing equations see Kundu et al. [46, Chap. 4]. However due to the velocity fluctuations, the system of equations is not in closed form. In fact, in LES, the GS motion or eddies that are associated with the length scales larger than the cut-off filter length (Δ) are explicitly simulated using relatively coarse mesh and large time-steps whilst the average effects of the SGS motion on the GS motion is accounted for by the SGS model [47]. Therefore, the one-equation eddy-viscosity model [48] is used in order to resolve the sub-grid kinetic turbulent energy (k_{sgs}). The transport equation for the SGS turbulent kinetic energy in one-equation eddy-viscosity model is

$$\frac{\partial k_{sgs}}{\partial t} + \nabla(k_{sgs}\overline{\mathbf{U}}) = 2\nu_{sgs} \parallel \mathcal{D}_{im} \parallel^2 - C_e\frac{k_{sgs}^{3/2}}{\Delta} + \nabla(\nu_{sgs}\nabla k_{sgs}) + \nu\nabla^2 k_{sgs}, \tag{3}$$

where $\overline{\mathbf{U}}$ denotes the LES-filtered velocity vector in x, y or z-direction, $\mathcal{D}_{im}$ is the filtered strain rate tensor, $C_e = 1.048$, $\nu_{sgs} = C_k\Delta\sqrt{k_{sgs}}$ is the sub-grid-scale kinematic viscosity, and C_k is 0.094. For more details on the derivation of (3) see [48] or [45]. Mukha and Liefvendahl [49] argues that, by solving for (3) the unresolved scales adjacent to the wall do not show the expected behavior based on the boundary layer theory. In order to rectify this misbehavior, the Van Driest damping function [50] is used in the solver. The domain discretization and solution of the governing equations, including Eq. (3), are done using `pisoFoam` solver in OpenFOAM (Open Field Operation and Manipulation) [51]. OpenFOAM uses finite volume method for discretization of the partial differential equations; details of the finite volume method along with validation and performance evaluation of the `pisoFoam` solver in turbulence modeling are presented in Versteeg and Malalasekera [52], and Dietzel et al. [53], respectively. In this regard, any validated model that can adequately resolve the velocity field in both space and time would be useful. However, OpenFOAM is adopted as it can be easily replaced by FireFOAM, which is a subset of OpenFOAM, once the combustion effects were to be coupled with the transport model. It is also very flexible in terms of dealing with complex geometries (unstructured domain discretization) which will be the case when the model is used for investigating firebrand shower scenarios in real WUI communities with complex terrain. For more information on the potential and capabilities of FireFOAM over other widely-used fire models see Maragkos et al. [54,55] and Maragkos and Merci [56].

2.3.2. Jet in non-uniform cross-flow (JINCF)

Given the sensitivity of firebrands transport to the characteristics of the velocity field, the effects of spatial and temporal velocity fluctuations in the wind tunnel experiments, which models a jet in non-uniform (boundary layer) cross-flow (JINCF), are simulated using LES. From nine cases of the wind tunnel experiments, LES of two cases are modeled which delivers simulation of six firebrand shower scenarios, as three different aspect ratio of model firebrands are released through each JINCF velocity field. Specifics of the conducted simulations are given in Tables 1 & 2. For a jet in a cross-flow, the height $z_m = \gamma/D$ is the height at which the jet becomes significantly bent over by the cross-flow. Values of z_m for the simulated velocity fields, i.e. case (1) and (2), are 0.615 and 0.639 m, respectively. For a jet in a boundary layer, as opposed to uniform, cross-flow the plume bends over more rapidly. The ratio of the bend over height for a jet in a uniform and boundary layer cross flow is given by ξ_m. For $\xi_m > 1$ the effects of the boundary layer velocity profile on the jet flow must be considered in any analysis. See Tohidi and Kaye [40] for more details. In this regard, values of ξ_m in Table 2 indicate that, it is necessary to consider the vertical gradient of the boundary layer for the LES of the wind tunnel experiments [40]. Given this, the inlets of precursor domains were fed with the experimentally measured velocity profiles shown in Fig. 3. The velocity fluctuations were generated using the digital filtering method of Klein et al. [58] which not only produces accurate turbulence intensities inside the domain but also significantly reduces the required length for the flow to develop [57]. For achieving better coherent structures, here, the development time, in precursor simulations, is considered to be after 10 flow revolutions in the channel flow as the streamwise dimension of the domain is larger. Then, a copy of the developed velocity profiles were used as boundary conditions for the main computational domain through outlets of the precursor domains and, the exact same profiles were fed to the inlets. These cyclic patches are shown in Fig. 5-(right). By adopting periodic boundary conditions for precursor domains, it is ensured that the fully developed flows were statistically stationary and statistically one-dimensional where, statistics of the velocities vary only in the z and x-directions, respectively for the channel and pipe flow [47].

Since JINCF velocity fields of the wind tunnel experiments are being simulated, the rest of the boundary conditions are adopted such that the side walls as well as the floor and ceiling are all considered to be of Dirichlet type, i.e. no-slip. Also, the ending face (outlet) of the domain, where the wind tunnel test section opens to the ambient and outflow condition occurs, the pressure is set to be zero. This implies that the obtained pressure field is relative to the ambient. For outflow conditions, the velocity gradient normal to the outlet $\partial U/\partial n +$ is set to be zero while no inlet flow is allowed inside through the outlet, i.e. $U_{n-} = 0$. This mixed boundary condition in OpenFOAM terminology is called `inletOutlet`. The prescribed inlet-outlet condition is also implemented on the resolved turbulent kinetic energy (k_{sgs}). The boundary conditions are summarized in Table 3. With regard to the spatial discretization of the domain, simple geometry allows for employing structured hexahedral cells, out of the jet bounding box, which can be easily refined close to the walls. However, since the passive lofting and downwind transport of model firebrands occurs far from the walls, there is no need for high resolution of the velocity scales near walls of the wind tunnel test section. Hence, the maximum mesh size is chosen to be equal to the smallest dimension of model firebrands, that is 0.01 m. This implies that the smallest resolved eddies are not larger than the smallest model firebrand ($\eta = 1$) tested. Also, for the jet bounding box, a parametric O-Grid mesh with, respectively, corner and arc stretch coefficients of 0.77 and 1.05 was used. As a result, in $x - y$ plane, $\Delta(x, y)_{min} = 0.000438$ m adjacent to the pipe's wall, and $\Delta(x, y)_{max} = 0.00268$ m at the centerline cells. The cell size in the z-direction conforms the mesh size argument out of the jet bounding box, that is $\Delta z = 0.01$ m. The aforementioned cell sizes are adopted according to the mesh convergence studies conducted for the precursor simulations, where the current sizes resolve velocity profiles with an overall error of less than 5% with respect to the experimentally measured velocities. Further, using the current mesh scheme for LES of case (2) in Table 1, the L^2-norm of the relative error for the resolved boundary layer velocity profile is 1.47%. The adopted mesh schemes, result in 11,696,860 cells just in the wind tunnel test section. Given the mesh sizes, the initial time-step (Δt) is calculated such that the Courant number is less than one [59]. Therefore, respectively, 1.5×10^{-4} s and 4×10^{-5} s were chosen as Δt for LES of case (1) and (2) in Table 1. Moreover, the adaptive time-stepping capability of `pisoFoam` solver, automatically, adjusts the run time Δt to keep the Courant number throughout the simulation time either smaller than one or equal to a predefined value, here 0.9; see OpenFOAM user guide. In order to couple the transport model with the resolved velocity field, a quasi-

Table 1
Parameters of the LES simulations. Here, ID is the case identification number, U_b is the bulk velocity of the boundary layer profile, Re_b is the corresponding bulk Reynolds number. Also, $U_{j,b}$ and $Re_{j,b}$ show the corresponding bulk velocity and Reynolds number for the jet.

ID	Boundary Layer					Jet			
	$U_0(m/s)$	$z_0(m)$	α	$U_b(m/s)$	Re_b	$U_{j\|r=0}$	$D(m)$	$U_{j,b}(m/s)$	$Re_{j,b}$
1	2.23	0.04	0.16	3.22	2.0857×10^5	9.00	0.152	2.919	1.4194×10^4
2	2.85	0.04	0.19	4.42	2.8657×10^5	12.00	0.152	3.998	1.9377×10^4

Table 2
Important parameters of the JINCF simulations, where μ is the velocity ratio, and ξ_m denotes the non-dimensional bending parameter of the jet through the boundary layer; see Tohidi and Kaye [40]. Also, the turbulent fluctuations flushing time based on characteristics of the boundary layer and jet are, respectively $\tau_{B.L.}$ and τ_j; see Ruiz et al. [57].

ID	Important parameters in LES of JINCF			
	$\gamma = U_0/U_{j\|r=0}$	$\tau_{B.L.} = l_x/U_0(s)$	$\tau_j = h/U_{j\|r=0}(s)$	ξ_m
1	0.247	2.24	0.226	1.56
2	0.238	1.75	0.169	1.71

Table 3
Summary of the implemented boundary conditions in LES of the wind tunnel test section. Here, P.S.C.F. and P.S.P.F. denote that the values are imported from the precursor simulations of the channel and pipe flow, respectively. Also, the presented velocity profiles at inlet patches are just to show the form of the averaged velocity distributions, although the values were imported from their corresponding precursor LES. Here, n denotes the outward normal vector the patch surface.

Patch name	$\overline{\mathbf{U}}$	$\overline{P}$	k_{sgs}	ν_{sgs}
Inlet boundary layer	$U_0\left(\frac{z}{z_0}\right)^{\alpha}$	P.S.C.F	P.S.C.F	P.S.C.F
Inlet jet	$U_{j\|r=0}e^{-4r^2/D^2}$	P.S.P.F.	P.S.P.F.	P.S.P.F.
Floor & ceiling	0	$\partial\overline{P}/\partial n = 0$	0	$\partial\nu_{sgs}/\partial n = 0$
Side walls	0	$\partial\overline{P}/\partial n = 0$	0	$\partial\nu_{sgs}/\partial n = 0$
Outlet	$\partial\overline{U}/\partial n += 0$, $U_{n-} = 0$	0	$\partial k_{sgs}/\partial n += 0$ $k_{sgs,n-} = 0$	$\partial\nu_{sgs}/\partial n = 0$

steady state must be reached. Therefore, the results are recorded after $20\tau_j$ seconds from the start of simulations with 0.01 s intervals. This optimum flush time allows for both flow types to extrude over the domain and initial turbulent intensities to flush out. The JINCF velocity field is, then, recorded for 3 s. More details on the precursor simulations, boundary conditions, mesh convergence studies, and LES setups can be found in Tohidi [23].

The simulations are carried out utilizing 800 Intel Xeon E5-2680v3 Central Processing Units (CPU) on Clemson University's Palmetto Cluster. Three seconds of simulation (after the flushing time) for case (1) and (2) required, respectively, 5.1876×10^6 s and 7.0433×10^6 s of CPU time. The post-processing is done using `paraview` with 10 NVIDIA Tesla-M2075 Graphical Processing Units (GPU). In Fig. 6, the resolved velocity profiles in the boundary layer and the jet are compared with experimental measurements in wind tunnel experiments. As can be seen in Fig. 6, there is a very good agreement between the experimentally measured velocity profiles and the corresponding LES resolved velocities. The discrepancies between the power-law fits and resolved velocities of the boundary layer adjacent to the ceiling of the wind tunnel (computational domain) are due to the implemented no-slip boundary condition at the ceiling patch of the computational domain. Also, the topology of the simulated flows is consistent with previous studies [57], in that the four main classes of vortices in JINCF, i.e. Ring-, Horse-shoe, V-shape, and Counter-rotating vortices, are all resolved. These coherent structures (except the Ring-vortex) are obtained by applying the Q-criterion on the LES-resolved velocity field of case (2); see Fig. 7.

Given that the captured velocity fields are accurate, the transport model is, then, coupled with the fully deterministic 3D 6-D.O.F. firebrand/debris transport model of Richards [30]. The coupling procedure is done by extracting the instantaneous and time-averaged velocity field data from LES along with the computational mesh information, namely position of nodes, and cell-centers. Through the coupling process, physical properties of the model firebrands including dimensions of the sides, aspect ratio, and density are assigned according to the wind tunnel experiments of Tohidi and Kaye [1]. The initial release angles (Tait-Bryan angles) are chosen randomly from a uniform distribution of $0 - 360°$. Similarly, the initial position of the release is seeded randomly from a uniform distribution of x and y coordinates through a circular plane of the jet nozzle at $z = 5$ mm (effective thickness of the model firebrands) with radius R. Subjecting the initial orientation of model firebrands as well as their initial location through the jet nozzle exit leads to random selection of their initial relative velocity such that sensitivity to release orientation and location in the experiments are captured in the model. An algorithm has been developed that calculates the relative velocity of the firebrands by subtracting their instantaneous velocity from the interpolated ambient velocity vector. The interpolation is done, spatially, based on the position of the centroid of the model firebrands in the computational mesh such that it finds the bounding cell where the centroid is located, at each time step. This is done for all three components of the velocity vector. As for of the temporal coupling, the time step in the transport model is chosen to be 1/10 of the time interval during which the LES data is stored (0.01 s). This means that the velocity field between these intervals is assumed to be steady. Then, the transport Eqs. (1) & (2) are integrated through time and the three dimensional locus of the centroid of the model firebrands (trajectory) during the lofting and downwind transport are reported as the final results.

3. Results

Specifics of the coupled numerical simulations are shown in Table 4. A set of simulations with different release radii (R) through the jet nozzle area are conducted in order to evaluate the sensitivity of the results to initial location of the firebrands in the velocity field. Also, effects of using a steady time-averaged velocity field, as opposed to using the LES-resolved velocity fields, on the trajectory of the model firebrands are investigated. A qualitative comparison between trajectories captured in lofting and downwind transport experiments and their corresponding simulations, using the developed coupled stochastic model, is shown in Fig. 8. The experimentally obtained and numerically resolved trajectories represent random release of model firebrands with $\eta = 4$ through a circular area ($R = 0.05$ m) of the jet nozzle exit in the JINCF, where interactions of boundary layer with $U_0 = 2.23$ m/s and jet with $U_{j|r=0} = 9$ m/s generate the velocity field. As can be seen in Fig. 8, the geometric form of the obtained trajectories, namely the trajectory curves, are the same as the experimental data. Nonetheless, sensitivity of the transport model to the initial coordinates of the release, and difference in the number of released model firebrands, 600 in simulations, relative to 126 experiments, have led to

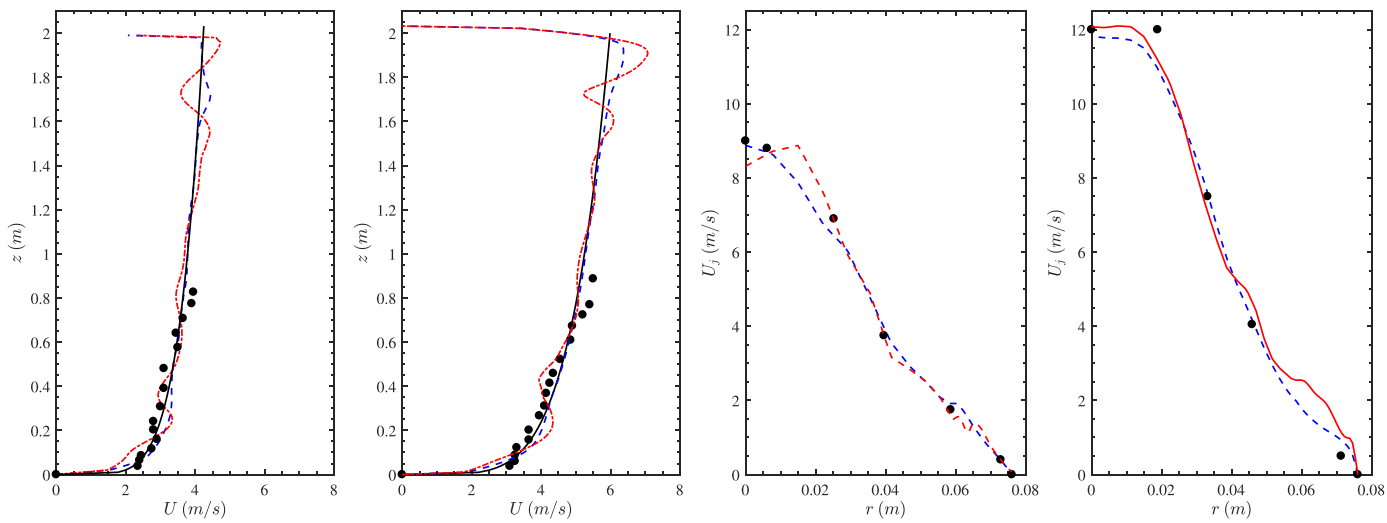

Fig. 6. Comparison between the experimentally measured (circles) velocity profiles of the boundary layer (far and middle left with U_0 = 2.23 m/s and 2.85 m/s, respectively) and the jet (middle and far right with $U_{j|r=0}$ = 9 m/s and 12 m/s, respectively) with their corresponding LES resolved profiles. The solid black lines show power-law fits to the boundary layer velocity profiles, double-dashed red and dashed-blue lines denote the instantaneous the time-averaged LES resolved velocity profiles, respectively. (For interpretation of the references to color in this figure legend, the reader is referred to the web version of this article.)

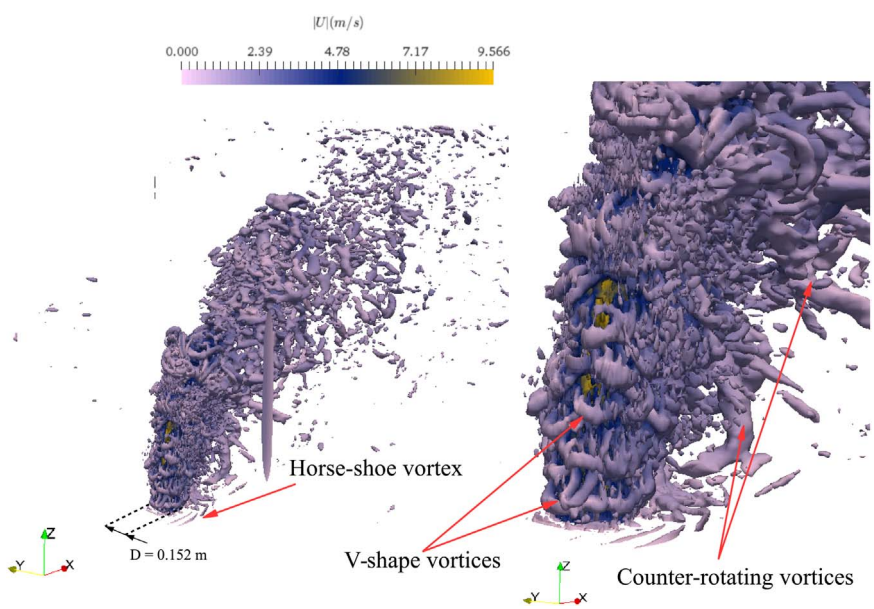

Fig. 7. (Left) obtained coherent structures of the JINCF in case (2) with iso-surfaces of the Q-criterion [60] where Q=175, and iso-surfaces are color coded with instantaneous velocity contours; (right) Close-up view of the iso-surfaces at near-field. Also shown is the jet nozzle exit diameter, i.e. D = 0.152 m, as the length scale. (For interpretation of the references to color in this figure legend, the reader is referred to the web version of this article.)

Table 4
Parameters of the coupled simulations. Here, D.O.F. is the number of model firebrands released through the LES resolved velocity fields, and R denotes the radius of the initial distribution of model firebrands within the jet nozzle area.

ID	η	D.O.F.	$R\,(cm)$
1	1	600	5.0
	4	600	5.0
	6*	600	5.0
2	1	600	5.0
	4	600	5.0
	6	600	0, 2.5, 5, 7.6

* Transport in this case is also simulated through a LES time-averaged velocity field.

more scatter in the landing location of the numerical results. More insight can be obtained by quantitative analysis of the results, shown in Fig. 9, where comparisons between numerical and experimental probability density function (PDF) and cumulative density function (CDF) of the normalized downwind distance (x_l/z_m) and the normalized maximum rise height (z_{max}/z_m) as well as the normalized downwind distance with the maximum rise height x_l/z_{max} are given. According to Fig. 9, there is a very good agreement between the experimental data and numerical results in estimating the mean value of the normalized parameters. Also, estimation of the variance is relatively good. This supports the adopted stochastic approach towards modeling the lofting and downwind transport of firebrands thorough the velocity field of a wildfire, despite the presence of uncertainties, and complexity of the phenomenon. The quantitative comparison between experimental data and numerical results is summarized in Fig. 10. This is done by calculating the mean (μ) and standard deviation (σ) of x_l/z_m and z_{max}/z_m for all six firebrand shower scenarios, presented in table 4, which are

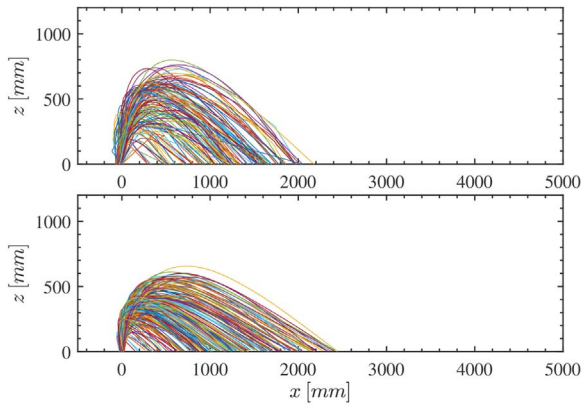

Fig. 8. Obtained trajectory of model firebrands with aspect ratio $\eta = 4$ from wind tunnel experiments (top) in relation to trajectories from corresponding simulations (bottom); The velocity field (JINCF) is generated by $U_0 = 2.23(m/s)$, and $U_{jlr=0} = 9.0(m/s)$.

modeled experimentally and numerically. Then, the obtained statistics of the experiments are drawn against the corresponding values from the numerical results. The results, as shown in Fig. 10, indicate that there is an excellent agreement between the estimated mean value of the normalized landing location and normalized rise height obtained from the simulations with the experimental data. In addition, there is a very small scatter around the line of $\sigma[z_{max}/z_m]$ (far-right in Fig. 10) which suggests that the model can estimate the second order statistics of the normalized lofted height with a small difference from the experimental data. This is invaluable as the maximum rise height is shown to have direct impact on the spotting distribution. As for of the $\sigma[x_l/z_m]$ the model is over estimating the variance in relation to the experimental data. This can be due to difference between the D.O.F. of experimental data (number of sample releases) and the number of released firebrands during the numerical simulations.

Through the experiments, the number of samples is low such that statistical hypothesis testing may not deliver robust results as the small DOF casts doubt about the credibility of the tests. This may be resolved by increasing the number of releases in experiments to the order of 1000, and conduct the numerical simulations with the same DOF. As it is shown by Tohidi [23], the transport model shows well-posed and bounded sensitivity to the added mass effects due to the rotational motion, and this delivers discrepancies (overestimation) in prediction of the standard deviation of the flight trajectories during free-fall. A possible source of discrepancy in σ may be associated with the duration of resolved ambient velocity field. In each experimental case, release of 200 model firebrands took approximately 480 s while LES simulations only provided 3 s of instantaneous velocity field due to limited computational resources. Considering that the model firebrands are released within the first second of simulations, in order for them to complete the lofting and downwind transport within the resolved time (3 s), there is significant difference in the release flux of the model firebrands. In fact, the release flux of the simulations, on average, is 1428 times that of the experiments. This suggests that the observed error in prediction of σ may be caused by the lack of content in the spatial and temporal variations of the stored velocity field through the LES [61]. Therefore, this issue may be tackled by reducing the release flux that can be achieved by longer record of the velocity field data, provided that the computational resources, especially enough memory, is available.

3.1. Sensitivity analysis

Simulations were, also, conducted for four different radii of the release area through the jet nozzle in order to demonstrate and quantify the sensitivity of the model to the initial coordinates of the release; see Table 4 for specific details. Fig. 11 illustrates the sensitivity of the results to the release radius by plotting PDFs of x_l/z_m and z_{max}/z_m. As can be seen on Fig. 11, increasing radius of the initial release for firebrands, increases the variability in the landing location, i.e. downwind distance, such that in $R = 5, 7.6$ cm the distributions are bimodal with smaller mean values and some upstream landing locations. The same behavior can be observed for the normalized maximum rise height where increasing the radius leads to more variability, and smaller average rise height; see Fig. 11-right.

These results imply that the model is sensitive to the initial coordinates of the release within the velocity field. In fact, one can infer the importance of firebrand break-off and formation, and their direct impact on the flight characteristics from here. Given these results, it is reasonable to believe that, the difference between the

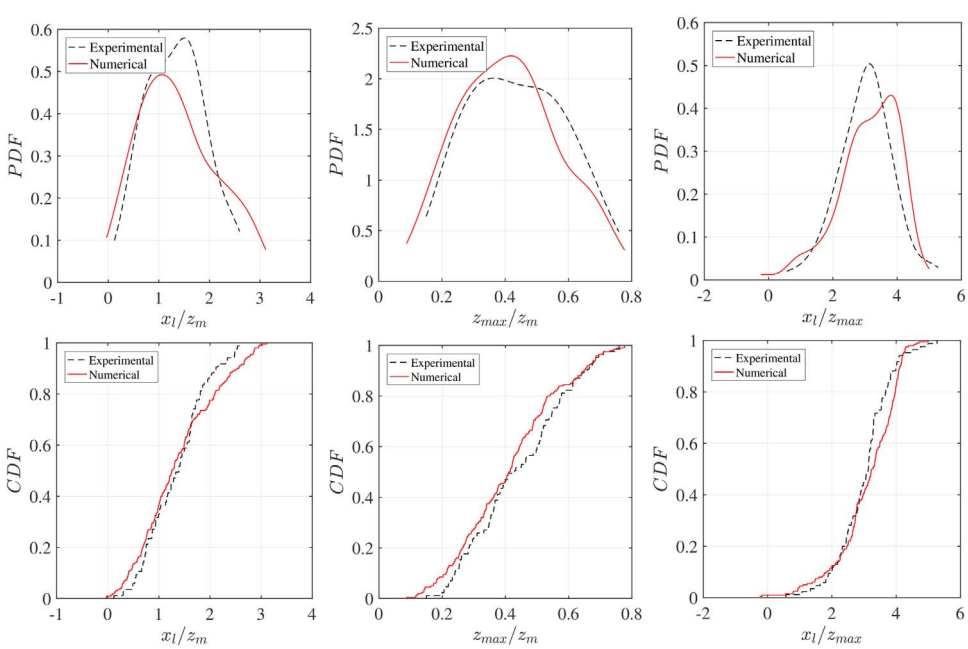

Fig. 9. Shown are PDF (top) and CDF (bottom) plots of the x_l/z_m (left), z_{max}/z_m (middle), and x_l/z_{max} (right). These plots correspond to the release of $\eta = 6$ model firebrands through the JINCF velocity field generated by $U_0 = 2.23(m/s)$, and $U_{jlr=0} = 9.0(m/s)$.

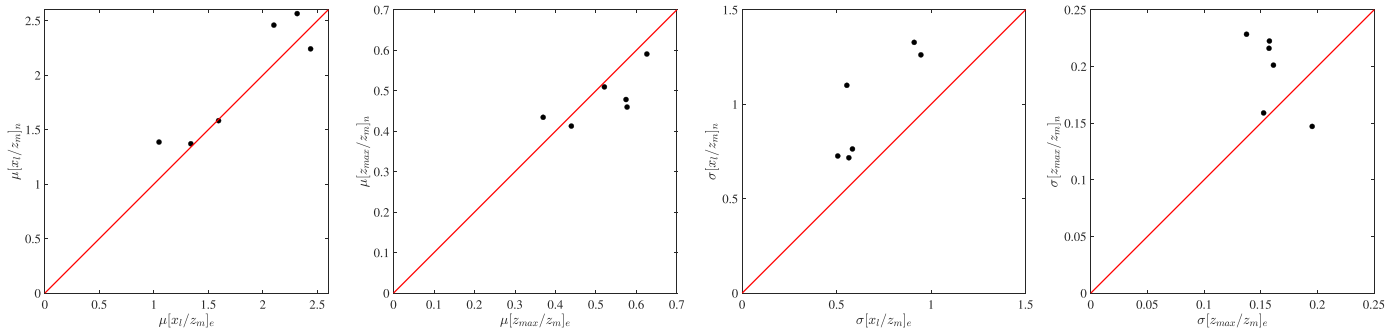

Fig. 10. Shown are the mean μ (far and middle left) and the standard deviation σ (far and middle right) plots of the x_l/z_m and z_{max}/z_m. The estimations based on the experimental data are drawn along horizontal axis and denoted with the subscript $_e$, whereas the numerically estimated results are given in vertical axis with subscript $_n$. Also, the red solid line has 1:1 slope. (For interpretation of the references to color in this figure legend, the reader is referred to the web version of this article.)

release radius in the experiments with the corresponding numerical simulations may have contributed to the overestimation of the variance in the numerical results as well. In this regard, as shown in Fig. 12, trajectories were spatially-averaged in the $x-z$ plane, in order to visualize the effects of release radius on the landing location and maximum rise height of the model firebrands through the numerical simulations compared to the spatially averaged trajectory of the corresponding experimental case. As it is evident in Fig. 12-left, increasing R exposes more firebrands to the lower jet velocities in relation to the jet centerline velocity. Therefore, the average maximum rise height decreases and subsequently the average maximum downwind distance decreases. In the wind tunnel experiment model firebrands were released from approximately the centerline of the jet. However, results of the image processing have shown that the brands are not exactly released from the centerline of the jet [23]. Hence, for consistency with experiments, $R = 5$ cm was adopted for all the numerical cases, even though Fig. 12-left shows that the release radius in experiments has been most likely less than 5 cm. Since these results are not known *apriori* for all cases, the choice of $R = 5$ cm is made based on the estimated operating radius of the individuals who conducted the experiments.

Finally, the response of the model to the use of a time-averaged (steady) velocity field instead of the LES resolved time-varying flow is investigated. To this end, the LES resolved velocity field of case (1) was time-averaged over 3 s and coupled with the transport model, and aspect ratio $\eta = 6$ model firebrands were released through this velocity field. The spatially-averaged trajectory of model firebrands, over 600 samples, is drawn versus the corresponding spatially-averaged trajectory that is obtained from using the LES-resolved velocity field; see Fig. 12-right.

Based on Fig. 12-right, there is a very little difference in estimating the maximum rise height. However, the difference is larger in estimation of the landing location. The mean landing location in the steady and unsteady simulations are 1098.2 mm and 1188.5 mm respectively, a difference of 8%. Also, the standard deviation of landing location obtained from steady and unsteady numerical simulations are 612.32 mm and 585.28 mm respectively, a difference of 5%. Since the standard deviations are close, a possible reason for such a small difference is the short period of time over which the velocity field is time-averaged. It is likely that by increasing the length of simulations from 3 s to the order of a couple of minutes at least, the resolved turbulent flow field would have enough content of the spatial (eddies) and temporal scales that will cause larger differences in the final trajectories, given that the transport model is highly nonlinear. However, quantification of the length of the simulations as well as subsequent offset error analysis in the simulations are not within the scope of this study.

4. Conclusion

Given the concerns raised at the beginning of the present study, about the simplifying assumptions embedded in model development procedures dealing with the simulation of firebrand shower scenarios and subsequent fire spotting, a coupled stochastic model of firebrand shower is developed. This model couples the fine resolution time-varying Large Eddy Simulation (LES) resolved velocity field of the jets/plumes in the non-uniform cross-flow boundary layers with the fully deterministic 3D 6-D.O.F. firebrand transport model. The development methodology is presented. It is shown that, the introduced probabilistic approach in modeling firebrands' flight is capable of estimating the first and second order statistics of the flight with adequate accuracy in relation to the wind tunnel experiments' data of Tohidi and Kaye [1], which represents the most comprehensive large scale experiments of lofting and downwind transport of rod-like model firebrands. Similar to

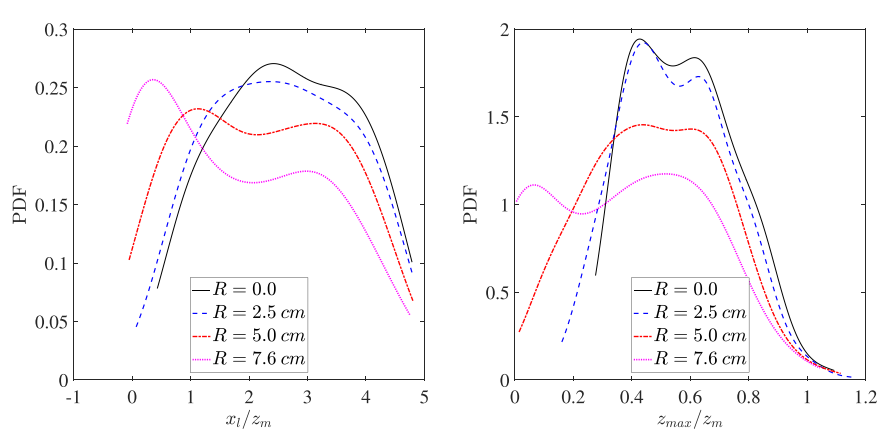

Fig. 11. Probability density function (PDF) of the x_l/z_m (left) and z_{max}/z_m (right) for different release radii of the model firebrands with aspect ratio $\eta = 6$ through the velocity field of case (2).

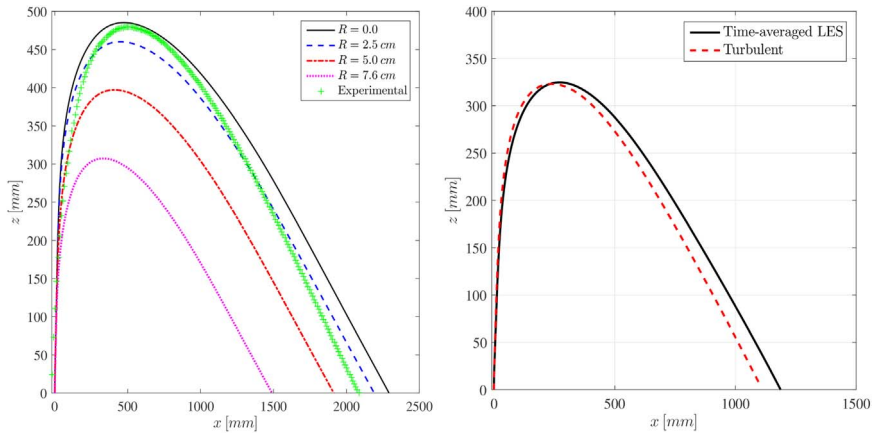

Fig. 12. On the left, shown are spatially-averaged trajectories, over 600 samples, of the model firebrands with aspect ratio $\eta = 6$ that are released, with different radii R, within the circular area of the jet nozzle in the velocity field of case (2). Also, the (green) symbolic line presents the spatially-averaged trajectory of the corresponding experimental case. On the right, shown is the side view comparison of spatially-averaged trajectories obtained from simulations through the time-varying turbulent velocity field of case (1) versus simulations in the 3-second-time-averaged velocity field of the same turbulent flow. (For interpretation of the references to color in this figure legend, the reader is referred to the web version of this article.)

the results of wind tunnel experiments, simulations, also, show that in modeling firebrand shower scenarios, the lofting cannot be decoupled from the downwind distance. Moreover, the sensitivity of the transport model to the initial release location was quantitatively explored. The sensitivity analysis results emphasize the need for experimentally validated models for firebrand formation and break-off, as the initial conditions of the flight significantly influence the lofting and downwind trajectories of firebrands and, ultimately, the spotting distribution. Further, the flight of firebrands is likely highly sensitive to the initial and boundary conditions that control the wind field. However, as the focus of this paper is on the development of an experimentally validated modeling approach such that our goal was to replicate the boundary conditions used in Tohidi and Kaye [1]'s experiments, such a detailed analysis was not undertaken. In the future, the application of this modeling approach to real wildfire situations would require the modeler to undertake an analysis of the sensitivity of their model prediction to their boundary conditions in order to quantify the uncertainty in their fire spotting predictions.

Acknowledgments

The authors would like to thank Meredith Frye and Alexandra Maass for their assistance with running the experiments and Danny Metz, Scott Black, and Sam Biemann for their help in building the test rig. This material is based upon work supported by the National Science Foundation under Grant no. 1200560. Any opinions, findings, and conclusions or recommendations expressed in the material are those of the author and do not necessarily reflect the views of the NSF.

References

[1] Ali Tohidi, Nigel Kaye, Comprehensive wind tunnel experiments of lofting and downwind transport of non-combusting rod-like model firebrands during firebrand shower scenarios. Fire Safety Journal, April 2017.
[2] Sara E. Sara, Raquel S.P. Hakes, Daniel J. Gorham, Aixi Zhou, Michael J. Gollner, Review of pathways for building fire spread in the wildland urban interface part i: exposure conditions, Fire Technol. (2016) 1–45 (ISSN 15728099).
[3] G Allard. Fire situation in the islamic republic of iran. International Forest Fire News (IFFN), 28: pp. 88–91, 2003.
[4] Ali Tohidi, Nigel Kaye, William Bridges, Statistical description of firebrand size and shape distribution from coniferous trees for use in Metropolis Monte Carlo simulations of firebrand flight distance, Fire Saf. J. 77 (2015) 21–35 (ISSN 03797112, URL ⟨http://linkinghub.elsevier.com/retrieve/pii/S0379711215300047⟩).
[5] William E. Mell, Samuel L. Manzello, Alexander Maranghides, David Butry, Ronald G. Rehm, The wildland-urban interface fire problem-current approaches and research needs, Int. J. Wildland Fire 19 (2) (2010) 238–251.
[6] Eunmo Koo, Patrick J. Pagni, David R. Weise, John P. Woycheese, Firebrands and spotting ignition in large-scale fires, Int. J. Wildland Fire 19 (7) (2010) 818 (ISSN 1049-8001, URL ⟨http://www.publish.csiro.au/?paper=WF07119⟩).
[7] N. Boonmee, J.G. Quintiere, Glowing and flaming autoignition of wood, Proc. Combust. Inst. 29 (2002) 289–296.
[8] M. Tachikawa, Trajectories of flat plates in uniform-flow with application to wind-generated missiles, J. Wind Eng. Ind. Aerodyn. 14 (1–3) (1983).
[9] M. Tachikawa, A method for estimating the distribution range of trajectories of wind-borne missiles, J. Wind Eng. Ind. Aerodyn. 29 (August (1–3)) (1988).
[10] J.D. Holmes, Trajectories of spheres in strong winds with application to wind-borne debris, J. Wind Eng. Ind. Aerodyn. 92 (1) (2004) 9–22 (URL ⟨http://dx.doi.org/10.1016/j.jweia.2003.09.031⟩).
[11] C.J. Baker, The debris flight equations, J. Wind Eng. Ind. Aerodyn. 95 (5) (2007) 329–353 (URL ⟨http://dx.doi.org/10.1016/j.jweia.2006.08.001⟩).
[12] P.J. Richards, N. Williams, B. Laing, M. McCarty, M. Pond, Numerical calculation of the three-dimensional motion of wind-borne debris, J. Wind Eng. Ind. Aero. 96 (2002) 2188–2202.
[13] Peter J. Richards, Nathan Williams, Brent Laing, Matthew McCarty, Michael Pond, Numerical calculation of the three-dimensional motion of wind-borne debris, J. Wind Eng. Ind. Aerodyn. 96 (October (10)) (2008) 2188–2202 (ISSN 01676105. URL ⟨http://linkinghub.elsevier.com/retrieve/pii/S0167610508000731⟩).
[14] Ralph A. Anthenien, Stephen D. Tse, A.Carlos Fernandez-Pello, On the trajectories of embers initially elevated or lofted by small scale ground fire plumes in high winds, Fire Saf. J. 41 (5) (2006) 349–363.
[15] Nicolas Sardoy, Jean-Louis Consalvi, Bernard Porterie, A. Fernandez-Pello, Modeling transport and combustion of firebrands from burning trees, Combust. Flame 150 (3) (2007) 151–169 (URL ⟨http://dx.doi.org/10.1016/j.combustflame.2007.04.008⟩).
[16] N. Sardoy, J.L.L. Consalvi, a. Kaiss, a.C.C. Fernandez-Pello, B. Porterie, a.C. Fernandez-Pello, Numerical study of ground-level distribution of firebrands generated by line fires, Combust. Flame 154 (August (3)) (2008) 478–488 (ISSN 00102180. URL ⟨http://linkinghub.elsevier.com/retrieve/pii/S0010218008001600⟩).
[17] S. Kortas, P. Mindykowski, J.L.L. Consalvi, H. Mhiri, B. Porterie, Experimental validation of a numerical model for the transport of firebrands, Fire Saf. J. 44 (November (8)) (2009) 1095–1102 (ISSN 03797112, URL ⟨http://linkinghub.elsevier.com/retrieve/pii/S0379711209001131⟩).
[18] Brent T. Visscher, Gregory A. Kopp, Trajectories of roof sheathing panels under high winds, J. Wind Eng. Ind. Aero. 95 (August (8)) (2007) 697–713 (ISSN 01676105. URL ⟨http://linkinghub.elsevier.com/retrieve/pii/S0167610507000128⟩).
[19] C.S. Tarifa, P. Notario, F.G. Moreno, On the flight paths and lifetimes of burning particles of wood, in: Proceedings of the Symposium (international) on combustion, volume 10, pp. 1021–1037. Elsevier, 1965.
[20] S.-L. Lee, J.M. Hellman, Firebrand trajectory study using an empirical velocity-dependent burning law, Combust. Flame 15 (3) (1970) 265–274.
[21] Sangay Bhutia, Mary Ann Jenkins, Ruiyu Sun, Comparison of firebrand propagation prediction by a plume model and a coupledfire/atmosphere largeeddy simulator. Journal of Advances in Modeling Earth Systems, 2: 4, mar 2010. ISSN 1942–2466. URL ⟨http://doi.wiley.com/10.3894/JAMES.2010.2.4⟩.
[22] Eunmo Koo, Rodman R. Linn, Patrick J. Pagni, Carleton B. Edminster, Modelling firebrand transport in wildfires using HIGRAD/FIRETEC, Int. J. Wildland Fire 21 (4) (2012) 396–417 (ISSN 1049-8001 URL ⟨http://www.publish.csiro.au/?paper=WF09146⟩).
[23] Ali Tohidi, Experimental and Numerical Modeling of Wildfire Spread via Fire Spotting. (Ph.D. thesis), Clemson University, 2016. URL ⟨http://tigerprints.clemson.edu/all_dissertations/1681/⟩.
[24] T. Himoto, K, Tanaka, Transport of disk-shaped firebrands in a turbulent boundary layer author, in: Proceedings of the Eighth International Symposium on Fire Safety

Science, pp. 18–23, 2005.
[25] J.E. Marte, D.W. Kurtz, G.H. Redmann, Aerodynamic coefficients of missile shapes, in: Proceedings of the Symposium on Tornadoes, pp. 623–631. Texas Tech University, USA, 1976.
[26] J.R Radbill, G.H Redman, Tornado-generated missile trajectory calculations with a six degree-of- freedom model, in: Proceedings of the Symposium on Tornadoes, pp. 633–637. Texas Tech University, USA, 1976.
[27] M. Tachikawa, H. Harra, Trajectories and velocities of typhoon-generated missiles, Part 3. Aerodynamic characteristics of various missile shapes, in: Proceedings of Transactions of the Architectural Institute of Japan, pp. 23–31, 1982.
[28] N. Lin, Simulation of windborne debris trajectories. (Ph.D. thesis), Texas Tech. University, 2005. URL ⟨http://repositories.tdl.org/tdl/handle/2346/1261⟩.
[29] Ning Lin, John D. Holmes, Chris W. Letchford, Trajectories of Wind-Borne Debris in Horizontal Winds and Applications to Impact Testing, J. Struct. Eng. 133 (February (2)) (2007) 274–282.
[30] P.J. Richards, Steady Aerodynamics of Rod and Plate Type Debris.pdf, in: Proceedings of the 17th Australian Fluid Mechanics Conference, 2010.
[31] Peter J. Peter, Dispersion of windborne debris, J. Wind Eng. Ind. Aero. 104–106 (May) (2012) 594–602 (ISSN 01676105. URL ⟨http://linkinghub.elsevier.com/retrieve/pii/S0167610512000505⟩).
[32] Michael Grayson, WeiChiang Pang, Scott Schiff, Three-dimensional probabilistic wind-borne debris trajectory model for building envelope impact risk assessment, J. Wind Eng. Ind. Aerodyn. 102 (March) (2012) 22–35 (ISSN 01676105. URL ⟨http://linkinghub.elsevier.com/retrieve/pii/S0167610512000037⟩).
[33] Jonathan Martin, Thomas Hillen, The spotting distribution of wildfires, Appl. Sci. 6 (6) (2016) 177 (ISSN 2076-3417. URL ⟨http://www.mdpi.com/2076-3417/6/6/177⟩).
[34] Hai-Hui H. Wang, Analysis on downwind distribution of firebrands sourced from a wildland fire, Fire Technol. 47 (2) (2011) 321–340 (URL ⟨http://dx.doi.org/10.1007/s10694-009-0134-4⟩).
[35] Frank A. Albini, Martin E. Alexander, Miguel G. Cruz, Miguel G. Cruz, A mathematical model for predicting the maximum potential spotting distance from a crown fire, Int. J. Wildland Fire 21 (1979) (2012) 609–627.
[36] J.D. Holmes, C.J. Baker, Y. Tamura, Tachikawa number: A proposal, J. Wind Eng. Ind. Aerodyn. 94 (1) (2006) 41–47.
[37] Samuel L. Manzello, Alexander Maranghides, William E. Mell, Thomas G. Cleary, Jiann C. Yang, Firebrand production from burning vegetation, For. Ecol. Manag. 234 (2006) (S119–S119).
[38] Samuel L. Manzello, Alexander Maranghides, William E. Mell, Firebrand generation from burning vegetation, Int. J. Wildland Fire 16 (4) (2007).
[39] Samuel L. Manzello, Alexander Maranghides, John R. Shields, William E. Mell, Yoshihiko Hayashi, Daisaku Nii, Mass and size distribution of firebrands generated from burning Korean pine (Pinus koraiensis) trees, Fire Mater. 33 (1) (2009).
[40] Ali Tohidi, Nigel B. Kaye, Highly buoyant bent-over plumes in a boundary layer, Atmos. Environ. 131 (2016) 97–114 (ISSN 13522310. URL ⟨http://linkinghub.elsevier.com/retrieve/pii/S1352231016300802⟩).
[41] Stephen D. Tse, A.Carlos Fernandez-Pello, On the flight paths of metal particles and embers generated by power lines in high winda potential source of wildland fires, Fire Saf. J. 30 (4) (1998) 333–356.
[42] B.W.W. Barr, O.a. Ezekoye, Thermo-mechanical modeling of firebrand breakage on a fractal tree, Proc. Combust. Inst. 34 (January (2)) (2013) 2649–2656 (ISSN 15407489, URL ⟨http://linkinghub.elsevier.com/retrieve/pii/S1540748912003586⟩).
[43] A. Karimpour, N.B. Kaye, On the stochastic nature of compact debris flight, J. Wind Eng. Ind. Aerodyn. 100 (1) (2012) 77–90.
[44] James W. Deardorff, A numerical study of three-dimensional turbulent channel flow at large reynolds numbers, J. Fluid Mech. 41 (02) (1970) 453–480.
[45] C. Fureby, A.D. Gosman, G. Tabor, H.G. Weller, N. Sandham, M. Wolfshtein, Large eddy simulation of turbulent channel flows, Turbul. Shear flows 11 (1997) 19–30.
[46] P.K. Kundu, I.M. Cohen, D.R. Dowling, Fluid Mechanics, Elsevier Science, 2015 (ISBN 9780124071513).
[47] S.B. Pope, Turbulent Flows, Cambridge University Press, 2000.
[48] Akira Yoshizawa, Kiyosi Horiuti, A Statistically-derived subgrid-scale kinetic model for the Large-Eddy Simulation of turbulent flows, J. Phys. Soc. Jpn. 54 (8) (1985) 2834–2839.
[49] Timofey Mukha, Mattias Liefvendahl, Large-eddy simulation of turbulent channel flow. Technical Report 2015-014, May 2015.
[50] Edward R Van Driest, On turbulent flow near a wall, Journal of the Aeronautical Sciences, 2012.
[51] H. Jasak, Z. Tukovic, A. Jemcov, OpenFOAM: A C ++ Library for Complex Physics Simulations ? In:Proceedings of the International Workshop on Coupled Methods in Numerical Dynamics, volume m, pp. 1–20, Dubrovnik, Croatia, 2007.
[52] Henk Kaarle Versteeg, Weeratunge Malalasekera, An introduction to computational fluid dynamics: the finite volume method, Pearson Education, 2007.
[53] Dirk Dietzel, Danny Messig, Federico Piscaglia, Andrea Montorfano, Gregor Olenik, Oliver T. Stein, Andreas Kronenburg, Angelo Onorati, Christian Hasse, Evaluation of scale resolving turbulence generation methods for large eddy simulation of turbulent flows, Comput. Fluids 93 (2014) 116–128.
[54] G. Maragkos, P. Rauwoens, B. Merci, Application of FDS and FireFOAM in large eddy simulations of a turbulent buoyant helium plume, Combust. Sci. Technol. 184 (July (7–8)) (2012) 1108–1120 (ISSN 0010-2202. URL ⟨http://www.tandfonline.com/doi/abs/10.1080/00102202.2012.664002⟩).
[55] G. Maragkos, P. Rauwoens, Y. Wang, B. Merci, B. Merci, Large eddy simulations of the flow in the near-field region of a turbulent buoyant helium plume, Flow. Turbul. Combust. 90 (90) (2013).
[56] G. Maragkos, B. Merci, Large eddy simulations of Fire CH4 fire plumes, Flow. Turbul. Combust. 6 (January) (2017) 36–42 (ISSN 1386-6184).
[57] a.M. Ruiz, G. Lacaze, J.C. Oefelein, Flow topologies and turbulence scales in a jet-in-cross-flow, Phys. Fluids 27 (4) (2015) 045101 (ISSN 1070-6631. URL ⟨http://scitation.aip.org/content/aip/journal/pof2/27/4/10.1063/1.4915065⟩).
[58] M. Klein, A. Sadiki, J. Janicka, A digital filter based generation of inflow data for spatially developing direct numerical or large eddy simulations, J. Comput. Phys. 186 (2) (2003) 652–665.
[59] Henk Kaarle Versteeg, An Introduction to Computational Fluid Dynamics the Finite Volume Method, 2/E, Pearson Education, India, 1995.
[60] Jeong Jinhee, Fazle Hussain, On the identification of a vortex, J. Fluid Mech. 285 (1995) 69–94.
[61] Julius S. Bendat, Allan G. Piersol, Random Data: Analysis and Measurement Procedures 729, John Wiley & Sons, 2011.